Materials Advances

ROYAL SOCIETY OF CHEMISTRY

PAPER

View Article Online
View Journal | View Issue

Check for updates

Cite this: *Mater. Adv.*, 2025, **6**, 8448

Received 30th August 2025,
Accepted 17th September 2025

DOI: 10.1039/d5ma00986c

rsc.li/materials-advances

Design and optimization of polyindole-integrated bimetallic composites (PLN/CuO–NiO and PLN/Mn–Cu) for efficient photocatalytic degradation of imidacloprid under sunlight irradiation

Muhammad Imran,[a] Amina Khan,[a] Raheeba Akbar,[a] Haq Nawaz Bhatti,*[a] Norah Alwadai[b] and Munawar Iqbal*[c]

The present study demonstrated the fabrication of novel polyindole (PLN)-based bimetallic nanocomposites (PLN/Mn–Cu and PLN/CuO–NiO) *via* coprecipitation, hydrothermal, and *in situ* polymerization methods for the photodegradation of imidacloprid (IMI) pesticide. Fourier transform infrared spectroscopy showed that PLN was successfully loaded onto the bimetallic nanocomposites' surface. X-ray diffraction analysis revealed that PLN/Mn–Cu exhibited a cubic phase with a crystallite size of 75 nm, while PLN/CuO–NiO retained cubic CuO and monoclinic NiO phases with a size of 54 nm. Scanning electron microscopy analysis showed that PLN/CuO–NiO featured spherical but irregular structures, while PLN/Mn–Cu exhibited a granular and uneven surface morphology. UV–visible analysis showed band gaps of 2.15 eV (PLN/Mn–Cu) and 2.13 eV (PLN/CuO–NiO), with strong absorption between 250 and 350 nm, confirming their visible-light photocatalytic potential. Photocatalytic activity of PLN/Mn–Cu and PLN/CuO–NiO composites exhibited 91% and 98% degradation efficiency of IMI pesticide under optimum conditions of pH = 10 and 4, catalyst dose = 5 mg L^{-1}, irradiation time = 120 min and 60 min, and pesticide dose = 2 and 6 mg L^{-1}, respectively. The kinetic study showed that the Behnajady–Modirshala–Ghanbery model fitted best with the experimental data. The study on reusability showed that catalysts can be used for five consecutive cycles. The work also demonstrates a sustainable and promising route for designing PLN-functionalized bimetallic nanocomposites for environmental remediation applications.

1. Introduction

Water is a vital and irreplaceable resource for sustaining life on the Earth. Human activities at every stage of development rely heavily on water, making it an essential element for growth and well-being, which resultantly are contaminating the water resources. There has been a rapid pollution of surface and groundwater during the last few years. Some of the global challenges of the 21st century are the rapid increase in population, expanding industrialisation, growing urbanisation, and increasing agricultural practices, all of which are contributing to a serious decline in superior water sources and lead to enormous wastewater production.[1] The major field in the world triggering water pollution is industrialization, discharging a large number of chemosynthetic materials with complex structures and high chemical stability into water sources.[2] These waste materials are harmful to aquatic life and human beings, especially when they encompass materials such as heavy metals, pesticides, pharmaceutical products and dyes, because they alter the pH and chemical composition of water and disturb the environmental balance.[3]

There is a high demand for pesticides worldwide as a consequence of growing agricultural activities, abolition of numerous infectious diseases and improvement in personal hygiene. Pesticides are classified as fungicides, nematicides, insecticides, rodenticides, weedicides, herbicides, algaecides, and bactericides, but the usage of herbicides and insecticides is 77% of the total pesticide usage in the world.[4] Of the 3.5 million tons of pesticides used throughout the world in a year,[5] only 1% reaches the target point, and the remaining 99% pollutes the soil and land and enters water resources through runoff and drainage.[6] Pesticides are posing serious threats to aquatic life and humans, causing cancer, neurological disorders, diabetes mellitus, cardiovascular disorders, reproductive syndromes and respiratory

---

[a] *Department of Chemistry, University of Agriculture, Faisalabad, Pakistan. E-mail: hnbhatti2005@yahoo.com*
[b] *Department of Physics, College of Sciences, Princess Nourah bint Abdulrahman University, P.O. Box 84428, Riyadh 11671, Saudi Arabia*
[c] *School of Chemistry, University of Punjab, Lahore, Pakistan. E-mail: Munawar.chem@pu.edu.pk*

disorders, because these mainly contain phenolic compounds in their composition, which are carcinogenic and mutagenic.[7]

Due to their good environmental compatibility, a broad spectrum of efficacy and targeted insecticidal toxicity, the most widely used group of pesticides is neonicotinoid insecticides.[8] Neonicotinoid insecticides are composed of two main compounds: nitro-substituted compounds (imidacloprid, clothianidin, thiamethoxam) and cyano-substituted compounds (thiacloprid and acetamiprid).[9] Imidacloprid (IMI) is one of the most common neonicotinoid insecticides, and its IUPAC name is 1-(6-chloro-3-pyridylmethyl)-*N*-nitroimidazolidin-2-ylideneamine ($C_9H_{10}ClN_5O_2$).[10] IMI is the first neonicotinoid insecticide and one of the extensively used chlorinated organic pesticides in the world.[11] This pesticide is present in 140 agricultural products and is most commonly used to control insects and pests in agriculture and landscaping as well as controlling termites and sucking insects in grassland and livestock in more than 120 countries in the world since its synthesis.[12] IMI is readily soluble in water (0.58 g L^{-1}), has more than 30 days of stability, is highly removable by photocatalysis, exhibits good environmental compatibility and possesses higher toxicity. IMI has two half-life spans: aerobic and anaerobic. The aerobic half-life is 2–3 hours, and the anaerobic half-life period is approximately 10–50 hours.[13] IMI accumulation is observed in surface water and wastewater at higher concentrations and at low concentrations in human beings. Therefore, it can affect the food chain and pose a serious threat to human health, such as cramps, fatigue, twitching and muscle weakness.[14] It is necessary to pass such pesticide pollutants from sewage before releasing them into water resources.

Conventional techniques adopted for treating pesticide pollutants are ozonolysis,[15] biological treatment,[16] sedimentation,[17] reverse osmosis,[18] chlorination,[19] activated carbon adsorption,[20] and filtration[21] *etc.*, but these methods have limitations in remediation process such as low efficacy, hazardous byproduct formation, incomplete removal of pollutants, high energy consumption and high cost of maintenance, *etc.*[22] However, recent technology has proposed the use of advanced oxidation processes (AOPs), such as photocatalysis, to generate reactive oxygen species in the presence of daylight and a semiconducting material for the photodegradation of organic pollutants into H_2O, CO_2 and inorganic ions.[23] With photocatalysis, the combination of two divergent metals to form a bimetallic nanocomposite (BNC) results in remarkable properties, including large surface area and reactivity, antibacterial property, nanosize and greater ability to catalyze reactions. Among various semiconductor-based bimetallic nanocomposites (BNCs), transition metals and their oxides such as copper oxide–nickel oxide (CuO–NiO) and manganese–copper (Mn–Cu) have gained attention for photocatalytic applications. When combined with polyindole (PLN) to form PLN/CuO–NiO and PLN/Mn–Cu composites, these materials exhibit low band gap energies ($\approx$2.13 eV), large surface area, and enhanced catalytic, electrical, and optical properties, making them highly efficient photocatalysts.[24]

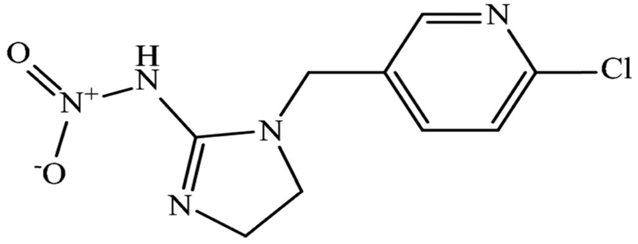

Fig. 1 Structure of imidacloprid.

Among various types of conducting polymers, PLN has displayed tremendous consideration during the last few years, especially due to its superior environmental stability, thermal stability, chemical stability, and one-dimensional nanostructure, and is considered a promising candidate for redox reactions compared to other polymers.[25] This polymer is excellent for applications in electronics, sensors, batteries, catalysis and coating.[26] Various approaches have been used to synthesize these nanocomposites, including precipitation,[27] hydrothermal methods[28] and *in situ* polymerization.[29] These synthesis methods are proven to be cost-effective, efficient, eco-friendly and free of any hazardous solvents. Thus, the present research has been designed to enhance the photocatalytic activity of Mn–Cu and CuO–NiO by reducing their band gap by modification with conducting polymer PLN. To be specific, Mn–Cu was prepared by the hydrothermal method, CuO–NiO was synthesized *via* the precipitation method, and PLN was synthesized and loaded on the surface of these BNCs using the *in situ* polymerization technique, and then employed for the photodegradation of IMI in aqueous media (Fig. 1).

2. Materials and methods

2.1 Materials

Copper nitrate trihydrate ($Cu(NO_3)_2\cdot 3H_2O$, 99%), nickel nitrate hexahydrate ($Ni(NO_3)_2\cdot 6H_2O$, 98%), zinc nitrate hexahydrate ($Zn(NO_3)_2\cdot 6H_2O$, 98%), ferric chloride hexahydrate ($FeCl_3\cdot 6H_2O$, 99%), sodium hydroxide (NaOH, 99%), indole (C_8H_7N, $\geq$98%) were purchased from Sigma-Aldrich (USA). Hydrochloric acid (HCl, 35%), ethanol (C_2H_5OH, $\geq$99%), methanol (CH_3OH, 99.8%) and potassium permanganate ($KMnO_4$, 99–100%) were procured from Merck (Germany) and citric acid monohydrate ($C_6H_8O_7\cdot H_2O$, 99.5%) was supplied by TTCA Co., Ltd (China). The analytical grade imidacloprid (IMI; $C_9H_{10}ClN_5O_2$, M_w = 255.7 g mol^{-1}, 98%) pesticide was obtained from Sigma-Aldrich (USA). All these analytical-grade chemicals were used without any further purification.

2.2 Synthesis of PLN/CuO–NiO

The co-precipitation procedure was used to prepare CuO–NiO BNCs. In the procedure, 0.2 M (40 mL) copper nitrate trihydrate solution was dissolved in 0.2 M (40 mL) nickel nitrate hexahydrate solution under magnetic stirring. Afterwards, 40 mL of 0.04 M citric acid monohydrate solution was prepared in deionized (DI) water and poured into the reaction mixture. Citric acid was utilized as a chelating agent to ensure the uniform distribution of metal ions, thereby preventing phase separation during thermal treatment and facilitating the formation of porous structures during calcination, which enhances the surface properties of the composites. After further stirring for 30 min, the addition of 1 M (150 mL) NaOH was carried out to adjust the pH of the solution to 5. Then, after further stirring for 1 h, the subsequent bluish-green precipitates were washed three times with DI water *via* centrifugation (4000 rpm) for 20 min to remove impurities. Next, the precipitates were dried at 70 °C for 16 h in an oven and calcined for 2 h at 400 °C in an electric furnace to obtain the CuO–NiO powder.[24]

The PLN/CuO–NiO was synthesized *via* an *in situ* polymerization technique using ferric chloride hexahydrate as a polymerizing agent. Ferric chloride hexahydrate ($FeCl_3{\cdot}6H_2O$) as a polymerizing agent initiates the oxidative polymerization of indole monomers, resulting in the formation of PLN chains on the surface of the composite. After being thoroughly washed, most iron species are eliminated, but elemental analysis shows that a small amount of residual Fe, which is strongly bonded to the polymer matrix, still remains in the final composites. Typically, in 50 mL of 1 N HCl solution, 1.3 g $FeCl_3{\cdot}6H_2O$ was dissolved and stirred for 30 min using a magnetic stirrer. Meanwhile, 0.2 g CuO–NiO was dispersed in 20 mL DI water and sonicated for 15 min. Then, the solution was transported into the reaction mixture and further stirred for 30 min. Then, 2 g of indole solution in 30 mL of ethanol was prepared and added dropwise into the reaction mixture with magnetic stirring for 24 h to start the polymerization process. Consequently, the resulting mixture was washed away with methanol and DI water *via* centrifugation (4000 rpm) for 20 min. Finally, the final product was dried at 70 °C for 24 h to obtain a fine powder (Fig. 2).[30]

2.3 Synthesis of PLN/Mn–Cu

A hydrothermal approach was employed to prepare Mn–Cu. In the reaction procedure, 0.3 M (40 mL) $KMnO_4$ and 0.5 M (40 mL) copper nitrate trihydrate solution were prepared in DI water under magnetic stirring for 20 min. Then, 0.1 M (40 mL)

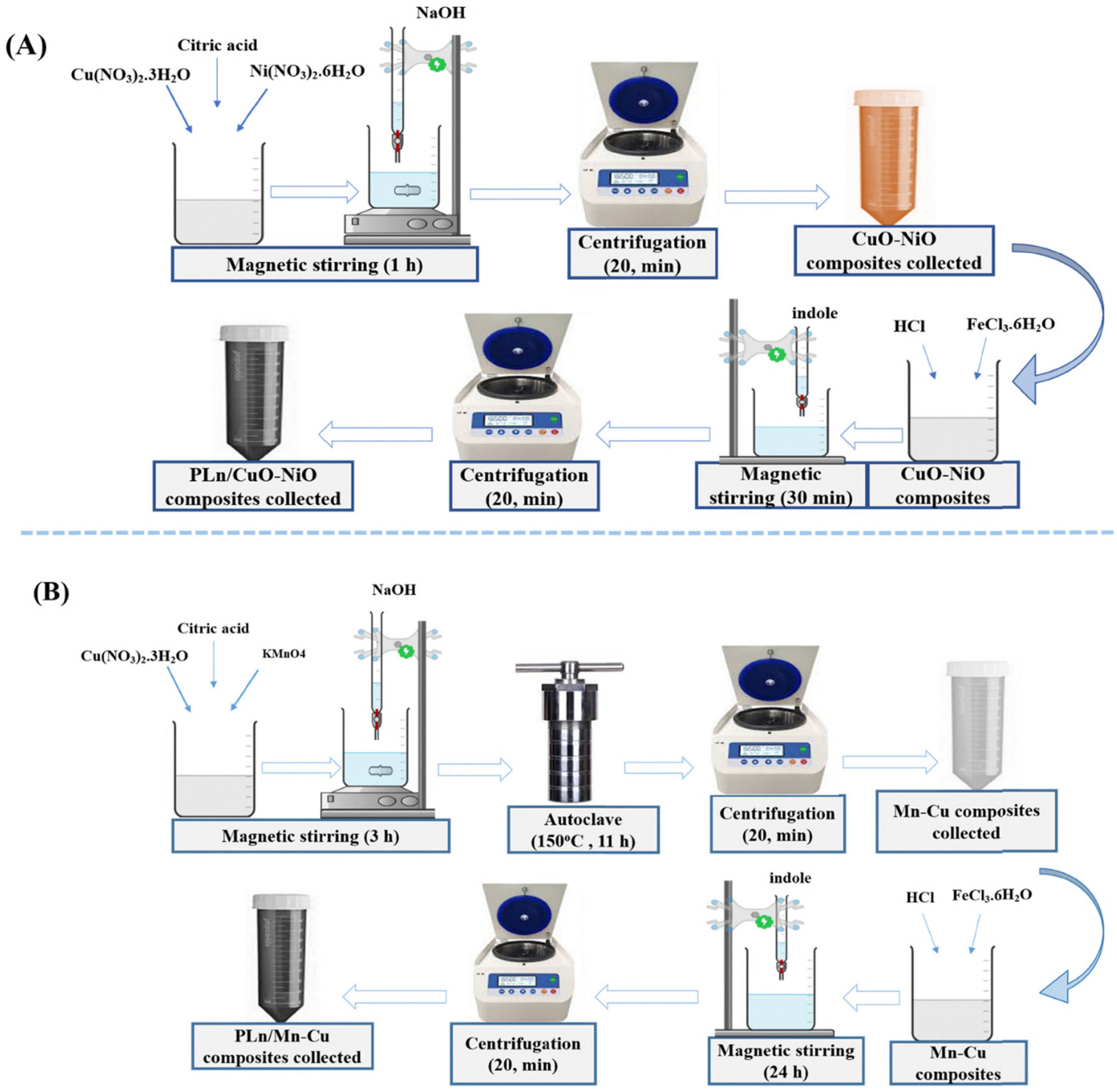

Fig. 2 Graphical representation for the preparation of (A) PLN/CuO–NiO and (B) PLN/Mn–Cu.

citric acid monohydrate was poured into the reaction mixture through magnetic stirring for 3 h. Afterwards, the mixture was transferred to a Teflon-lined stainless-steel autoclave (150 mL) and heated at 150 °C for 12 h. To ensure uniform metal ion distribution and to facilitate the formation of porous structures, citric acid monohydrate was added as a mild reducing agent and chelating agent. When heated in water under hydrothermal conditions, citric acid reduces $KMnO_4$ (Mn^{7+}) to MnO_2 and Cu^{2+} ions to Cu^+ or CuO, enabling the synthesis of mixed metal oxides with controlled valence states and preventing phase separation. The simplified reactions can be represented as follows:

$$2KMnO_4 + 5C_6H_8O_7 + 3H_2O \rightarrow 2MnO_2 + 5C_6H_6O_7 + 2KOH + 4HNO_3 \quad (1)$$

$$2Cu(NO_3)_2 + C_6H_8O_7 \rightarrow 2Cu^+ + 6CO_2 + 4H_2O + 4NO_X \quad (2)$$

Then, the precipitates were washed with DI water to remove impurities and dried at 70 °C for 11 h.[31] For the preparation of PLN/Mn–Cu, an *in situ* polymerization technique was used. Typically, 1.4 g $FeCl_3\cdot6H_2O$ was added to a 1 N HCl (50 mL) solution under magnetic stirring for 30 min. After that, 0.1 g Mn–Cu was dispersed in 20 mL DI water and sonicated for 20 min. Meanwhile, the solution was poured into the above reaction mixture and further stirred for 30 min to obtain a homogeneous dispersion. Next, 2 g of indole solution in 30 mL of ethanol was prepared and poured dropwise into the above mixture *via* magnetic stirring for 24 h. Subsequently, the obtained precipitates were washed with methanol and DI water *via* centrifugation (5000 rpm, for 20 min), and dried at 80 °C to obtain a final product (Fig. 3 and 4).[32]

2.4 Characterization

The surface study of the test samples was analyzed using scanning electron microscopy (FEI Nova Nano SEM) operated at 20 kV, connected to an EDX acquisition detector to determine the elemental composition.[33] The ultraviolet-visible absorption spectra of composites were recorded in the 250–900 nm range *via* a CE 7200 spectrophotometer, UK.[34] Functional group analysis of test specimens was carried out *via* extracted FTIR spectra in the 4000–650 cm^{-1} range using an Agilent (USA) Cary 360 Spectrophotometer.[35] The crystalline properties of the composites were obtained using a BRUKER D8 Model Powder Diffractometer (XRD) (USA) with (λ = 1.54 Å) at a scan range of 2θ = 10–80°, working at 30 mA and 40 kV.[36] From the XRD analysis, the average crystallite size of the prepared samples was calculated through Debye–Scherrer's formula (eqn (3)):

$$D = \frac{k\lambda}{\beta\cos\theta} \quad (3)$$

where k = shape factor, λ = 1.5406 Å, θ = Bragg's angle, and β = line broadening at half maximum intensity.

2.5 Photocatalytic procedure

The synthesized PLN/CuO–NiO and PLN/Mn–Cu were tested against IMI pesticide to determine their photocatalytic activity. To examine the photocatalytic process, reaction parameters were set as 2–12 pH, 5–30 mg L^{-1} of catalyst dose, 2–12 mg L^{-1} of initial dye concentration, and 10–160 min of contact time. The experiments were performed as follows: 0.01 g of the weighed composition of catalysts was poured into 100 mL of a 10 mg L^{-1} solution of imidacloprid pesticide with the addition of 10 mM of H_2O_2 as an oxidizing agent, and before irradiation with sunlight, the solution was first placed under dark light for 20 min to attain adsorption–desorption equilibrium. Then, the solution was put under direct exposure to visible light under shaking, working at 120 rpm. After a definite time interval, 5 mL of the test samples was taken from the reaction mixture and centrifuged at 4000 rpm for 15 min. The variation in IMI pesticide amount as a function of radiation time was examined using a UV-vis spectrophotometer by measuring the absorbance at λ_{max} of 270 nm. The IMI removal efficiency was calculated using eqn (4).

$$\text{Degradation } (\%) = \left(\frac{A_0 - A_t}{A_0}\right) \times 100 \quad (4)$$

where "A_0" and "A_t" indicate the initial (t = 0 min) and equilibrium (t = t minutes) concentrations (mg L^{-1}) of pesticide, respectively.

3. Results and discussion

3.1 FTIR analysis

FTIR study was used to identify the presence of functional groups on the external surface of the materials. The FTIR spectra of PLN, PLN/CuO–NiO and PLN/Mn–Cu were recorded in the range of 4000–650 cm^{-1} and the responses thus obtained are displayed in Fig. 4. The intense IR band located at 3390 cm^{-1} belongs to the characteristic NH stretching vibration of PLN, and the band at 1561 cm^{-1} is attributed to the deformational vibration mode of NH bond and the vibrational mode of C=C bonds in the aromatic ring of indole, respectively, as depicted in Fig. 4A. These studies specify the existence of NH bond in the polyindole ring and indicate that the nitrogen atom of indole is not involved in the polymerization process.[37] The peaks positioned at 1448 and 1328 cm^{-1} represent the C–N and C=N stretching modes of vibration of indole, respectively. The band positioned at 1094 cm^{-1} has been assigned to in-plane CH bonding modes present in the aromatic heterocyclic part of indole. The sharp band at 733 cm^{-1} corresponds to the CH bond out of plane distortion, and the peak around 720 cm^{-1} shows that the in-phase vibrational movement of hydrogen atoms at the 2 and 3 carbon site is missing.[38] These indications imply that the polymerization process does not occur at the benzene ring, and the 2, 3 position of pyrrole is responsible for the polymerization process.

The existence of a broad peak around 3400 cm^{-1} is ascribed to the OH stretching vibration of water molecules in the sample

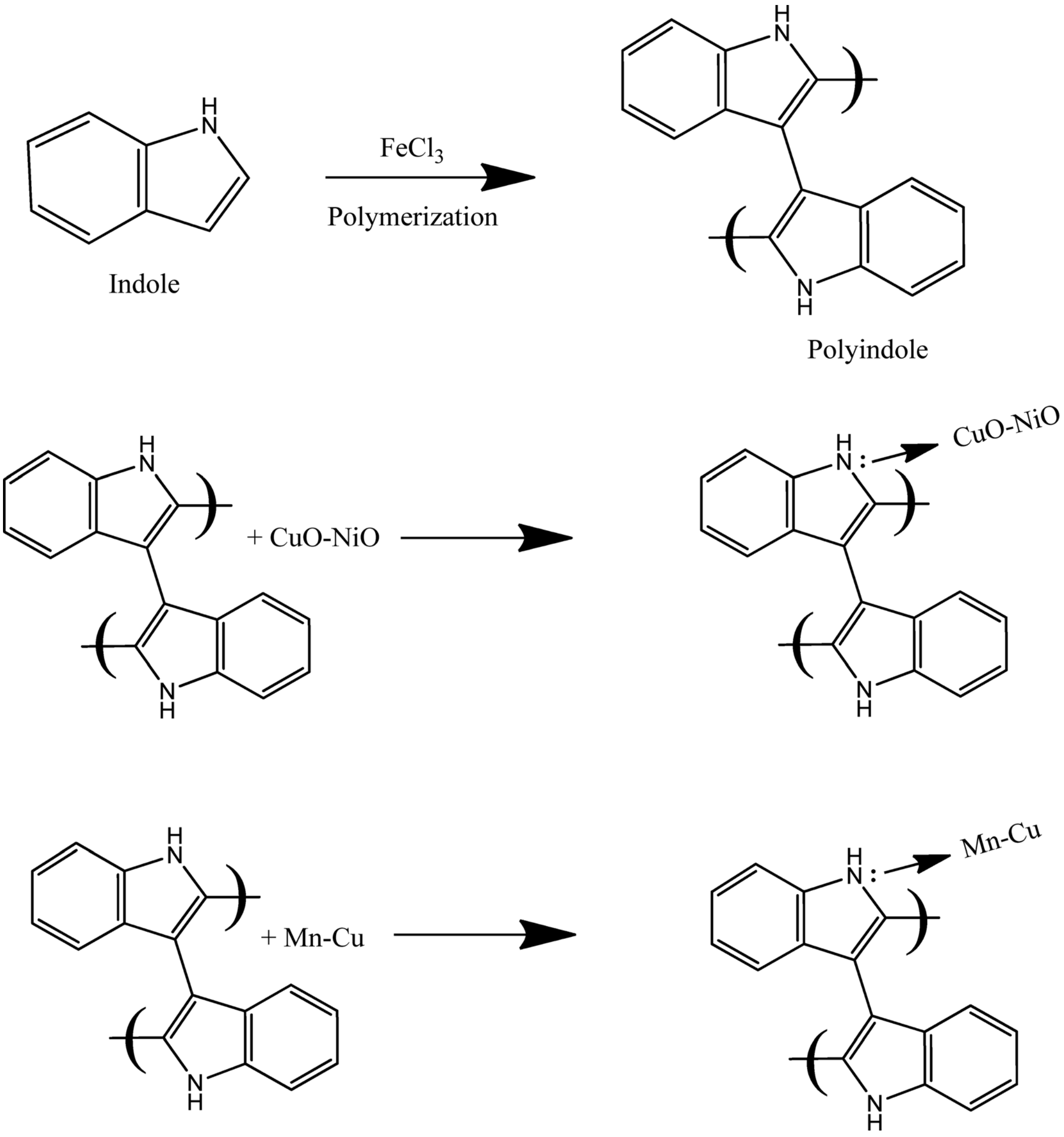

Fig. 3 Structural representation of the interaction mechanisms of PLN, PLN/CuO–NiO, and PLN/Mn–Cu.

of CuO–NiO, as shown in Fig. 4B. The peak appearing near 1600 cm^{-1} is attributed to the bending vibration of water adsorbed on the surface. The presence of a peak around 2300 cm^{-1} is indicative of the existence of CO_2 in the samples. Hence, a peak at 1127 cm^{-1} assigned to Cu–O–Ni interactions confirms the formation of nanoparticles. Furthermore, the two peaks identified at 1461 and 860 cm^{-1} corresponded to the metal oxide vibration modes in the sample.[39] Hence, FTIR spectrum confirms that the PLN/CuO–NiO has characteristic absorption bands at 3410, 2282, 1548, 1450, 1328, and 740 cm^{-1} for OH, CO_2, aromatic C═C, C–N, C═N, and C–H out of plane in benzene, respectively.[40] The results show that the peaks of polymer are blue-shifted, indicating that a covalent bond is formed between the polymer and the composite in the formation of PLN/CuO–NiO.

An intense peak at 3400 cm^{-1} is due to OH of absorbed water, and a peak around 3600 cm^{-1} reveals the Mn–OH vibration in the structure of Mn–Cu and PLN/Mn–Cu, respectively (Fig. 4C). A sharp band at 747 cm^{-1} is due to Mn–Cu–O, and the band at 1067 cm^{-1} is ascribed to the stretching mode of C–O in Mn–Cu.[41] A bifurcated peak around 1600 cm^{-1} arises due to the absorption of atmospheric CO_2 on the surface of nanoparticles. The bands that appeared at 1075 and 735 cm^{-1} are indicative of the C–H stretching mode of vibration in the structure of the benzene ring.[42] A slight shift in the wavenumber values in the spectrum of PLN/Mn–Cu reveals the interaction between the polymer and the composite material and validates the formation of PBNC.

3.2 Optical analysis

UV-vis spectroscopy helps to evaluate the absorbance, transmittance, and inner transition in the particles and their band gap study.[43] The UV-vis absorption spectra of the synthesized composites were recorded in the range of 250–900 nm, as shown

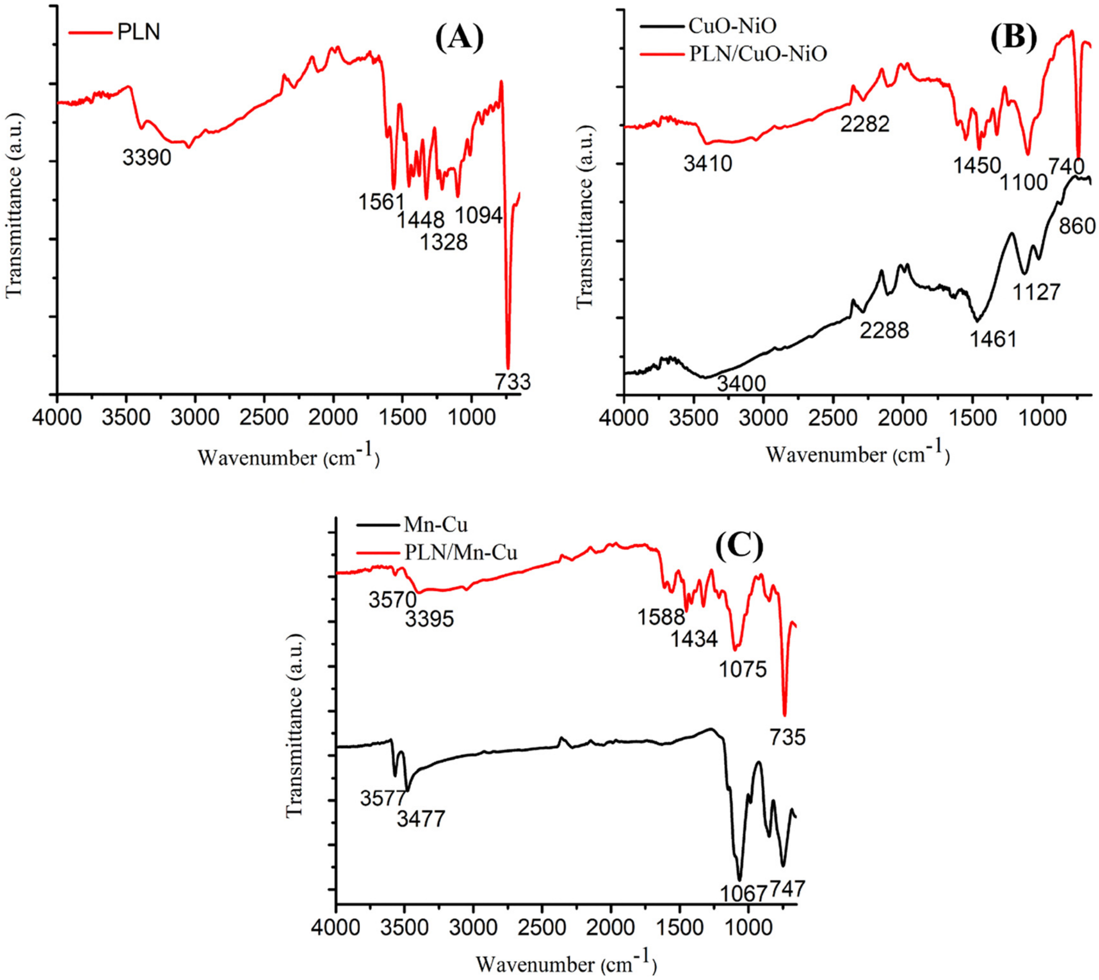

Fig. 4 FTIR spectra of (A) PLN, (B) CuO–NiO and PLN/CuO–NiO, and (C) Mn–Cu and PLN/Mn–Cu.

in Fig. 5. A strong absorption band of CuO–NiO was obtained at 250 nm in the ultraviolet region (Fig. 5A). The absorption rate of the composite decreased drastically with a blue shift due to the formation of CuO–NiO composite. The deposition of PLN into the composite resulted in a redshift of PLN/CuO–NiO at 304 nm.[44] The UV spectral peaks of Mn–Cu and PLN/Mn–Cu were evaluated at wavelengths of 275 and 280 nm, respectively (Fig. 5B). The sharpness and intensity of the UV-vis spectra indicate that the synthesized composites are nanosized.[45]

The difference in excitation energy from the valence band to the conduction band in a material under study is known as the band gap energy (E_g).[46] The photocatalytic efficiency of a composite depends upon its E_g value, which was determined from the well-known Tauc plot relation.

$$\alpha h\nu = Z(h\nu - E_g)^n \qquad (5)$$

Here, Z is the band tailing parameter, $h\nu$ is the energy of a photon, E_g is the nanoparticle band gap, and α is the absorption coefficient calculated by eqn (6).

$$\alpha = 2.303\frac{A}{d} \qquad (6)$$

Here, A is the absorbance and d is considered as sample thickness or cuvette path length. By plotting graphs between $(\alpha h\nu)^2$ and $h\nu$, the E_g value of the composites under consideration was calculated.[47] The photocatalysts having E_g values greater than 3 would absorb efficiently in the visible region and *vice versa*. From the Tauc plot, the values of the direct optical band gap were determined to be 2.38 eV for CuO–NiO, 2.13 eV for PLN/CuO–NiO (Fig. 5C), 2.34 eV for Mn–Cu, and 2.15 eV for PLN/Mn–Cu (Fig. 5D), respectively.[48] The optical bandgap value decreased with the addition of the polymer in to the composites, because of the generation of electrons that reduced the band gap.

3.3 Surface morphology

The surface morphology of the nanocomposites was studied with SEM analysis. The magnified images of the samples were taken at a 5 μm scale.[49] SEM images and histograms of PLN/CuO–NiO and PLN/Mn–Cu are depicted in Fig. 6. The image reveals that PLN/CuO–NiO composite displays predominantly spherical particles with some irregularities at the edges, indicating partial agglomeration (Fig. 6A). The Mn–Cu composite exhibits a granular morphology that is composed of small,

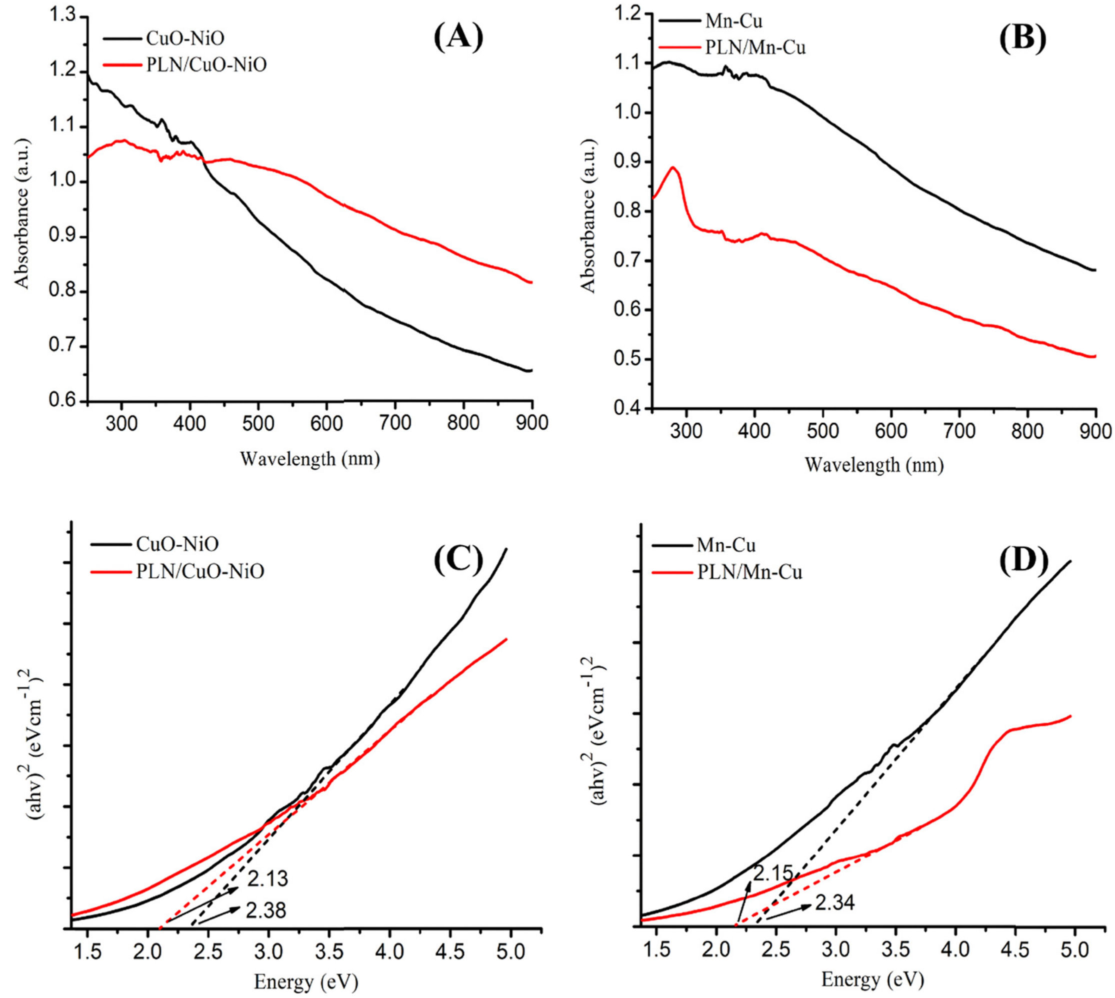

Fig. 5 (A) and (B) UV-visible spectra and (C) and (D) Tauc plots for the energy band gap of Mn–Cu in PLN/Mn–Cu and CuO–NiO in PLN/CuO–NiO.

irregularly shaped particles forming loosely packed clusters, giving a heterogeneous surface appearance, and showing the presence of PLN sheets in the sample (Fig. 6B). The slight presence of agglomeration is attributed to surface tension and high surface energy of the composites.[50] Meanwhile, Mn–Cu and CuO–NiO are uniformly distributed and cover the surface of PLN sheets, which confirms the existence of these nanoparticles on PLN sheets. From SEM images, it is evident that the incorporation of PLN into these nanocomposites provides enough surface area for electron transfer and increases reaction sites.[37] The SEM images of the composites were further examined by ImageJ software to determine their average particle size distribution. The average size distribution of the PLN/CuO–NiO is found to be 75 nm based on 120 measurements, as depicted in Fig. 6C. In contrast, from a total of 100 measurements taken, the average size for PLN/Mn–Cu was calculated to be 118 nm (Fig. 6D). Furthermore, this calculated size was higher than the average size determined from the Debye–Scherrer formula.[51] This difference is due to the effect of lattice strain on the crystal structure, which is not measured by the Debye–Scherrer equation.

3.4 XRD analysis

The XRD technique was used to examine the crystallinity and phase purity of the prepared composites, and the XRD pattern of the materials is depicted in Fig. 7. In the XRD pattern of PLN/Mn–Cu, the 2θ angles of 17.3°, 28.9°, 35.4°, 39.2°, 41.8°, 46.4°, 47.9°, 53.8° 56.7° and 68.5° were assigned to the (111), (200), (220), (311), (222), (400), (331), (422), (333), (315) lattice planes, attributed to the face-centered cubic structure of Mn_3O_4 (JCPDS no. 24-0734) and metallic Cu (JCPDS no. 04-0836) phases in the composite, with the presence of sharp intense peaks showing good crystallinity in the material, as shown in Fig. 7.[52] Furthermore, there are a few low-intensity diffraction peaks obtained at 2θ values of 19.2°, 24.2°, and 26.8°, which indicate the presence of PLN in PLN/Mn–Cu with an amorphous nature. The values of lattice parameters of the test specimen were obtained as a = 4.710 (Å), b = 4.710 (Å), and c = 4.710 (Å). The plane patterns (011), (111), (110), (020), (121), (022), (1 32) at 2θ values of 13.3°, 16.7°, 22.7°, 28.9°, 44.4°, 52.6°, 60.1°, 65.91°, respectively, correspond to PLN/CuO–NiO and match well with monoclinic CuO (JCPDS no. 45-0937) and the cubic structure of NiO (JCPDS no. 47-1049)[53] with values of lattice parameters observed in the

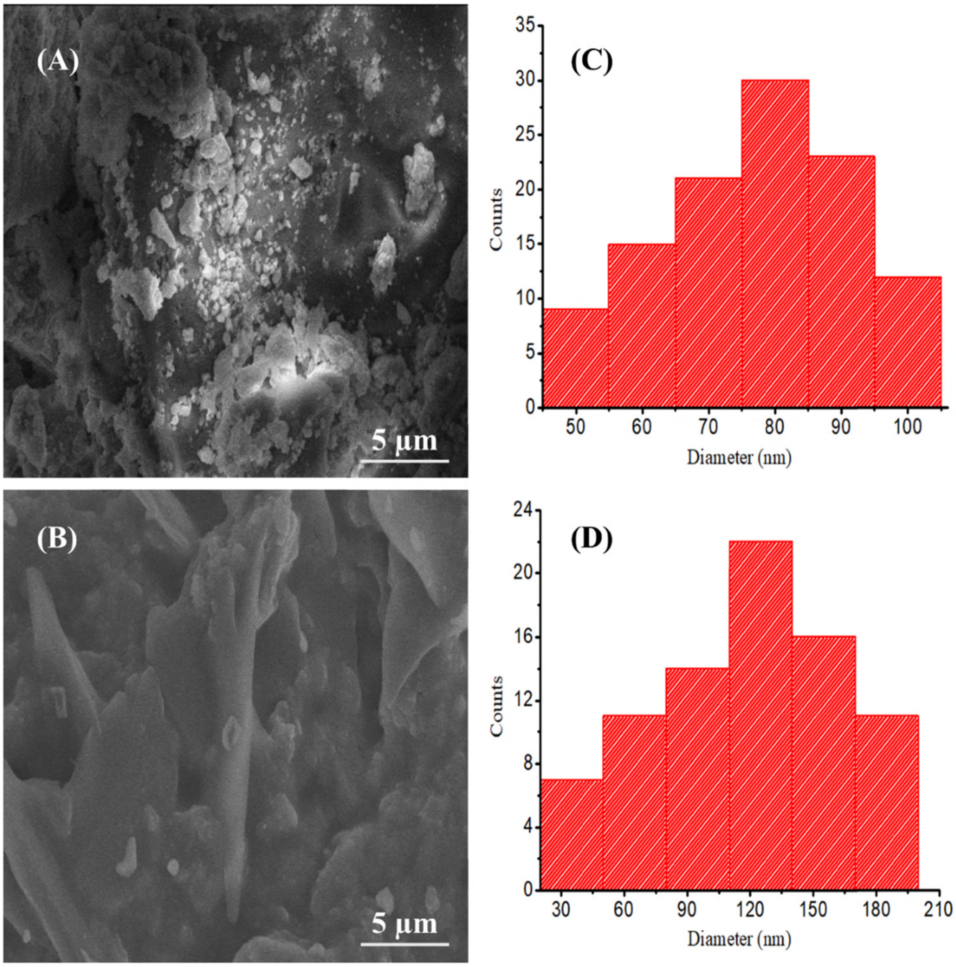

Fig. 6 SEM micrographs of (A) PLN/CuO–NiO and (B) PLN/Mn–Cu with corresponding size distribution histograms of (C) PLN/CuO–NiO and (D) PLN/Mn–Cu.

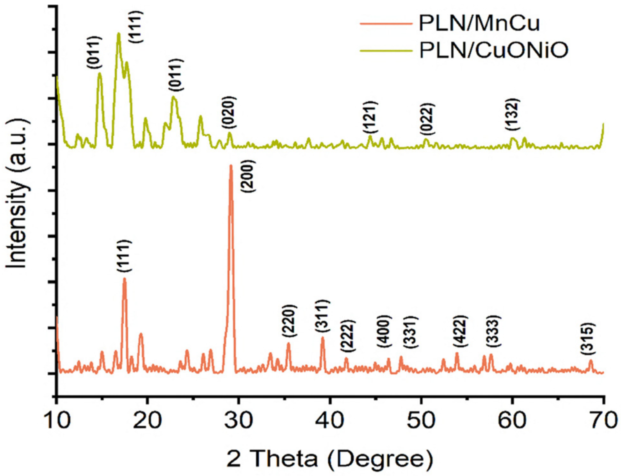

Fig. 7 XRD patterns of PLN/Mn–Cu and PLN/CuO–NiO.

composite as a = 4.2520 (Å), b = 4.2520 (Å), and c = 4.2520 (Å). The presence of intense peaks at 19.6° and 25.5° confirms the presence of PLN with a partial crystalline nature.[54] It is concluded that the existence of PLN peaks confirms its incorporation into the CuO–NiO composite. The sharp intensity peaks centered below 20° values demonstrate crystallinity in the composite material. The average crystal size of the composites was calculated using the Debye–Scherrer formula, based on the highest intensity peaks, that is (200) at 28.9° and (111) at 16.7° of the prepared PBNCs, respectively. The average crystal size was found to be 79 and 54 nm for PLN/Mn–Cu and PLN/CuO–NiO, respectively. The obtained results of lattice parameters and volumes of unit cells are illustrated in Table 1.

3.5 Photocatalytic performances

3.5.1 Effect of pH and point of zero charge (PZC) analysis. The surface catalytic properties of the BNCs and treated PLN could be explained in terms of the PZC, which is the point at which the charge on the surface of the catalyst becomes zero.[55] If the pHPZC is higher than the optimized pH of the composite, the composite surface will have a positive charge, and if the pHPZC is lower than the optimum pH, the composite surface will possess a negative charge. The catalyst surface charge helps determine the degradation capability of anions and cations.[56] Sodium chloride (NaCl) (0.1 M) solution was used to determine pHPZC, and the results are depicted in Fig. 8A. The pHPZC

Table 1 XRD data peaks for PLN/Mn–Cu and PLN/CuO–NiO

Phase	Lattice constants (Å)	Unit cell volume ($Å^3$)
Face centered-cubic (PLN/Mn–Cu)	$a = 4.710$ $b = 4.710$ $c = 4.710$	104.49
Cubic (PLN/CuO–NiO)	$a = 4.2520$ $b = 4.2520$ $c = 4.2520$	76.87

values were calculated to be 6.28 and 6.48 in the case of PLN/CuO–NiO and PLN/Mn–Cu, respectively.[57] The pH is the dominant parameter in the degradation procedure. By varying the pH, the interaction between composites and imidacloprid was altered, which was studied in the range of pH 2–12.

Imidacloprid is present in its neutral form, but its degradation is facilitated by reaction conditions, which can be accelerated in more acidic and alkaline environments.[58] The results indicated that maximum degradation capacities of 91% and 98% were achieved for the PBNCs at pH 4 and 10, respectively (Fig. 8B). It was observed that acidic pH was reliable for degradation using PLN/CuO–NiO under irradiation because in acidic pH, due to the higher concentration of H^+, the electrostatic attraction between the positively charged composite surface and negatively charged pesticide molecules will increase, and consequently, the degradation capacity will be enhanced, which can be explained using the pHPZC concept.[59] Under alkaline conditions, the surface of PLN/Mn–Cu changed to negatively charged at pH 10 due to the generation of hydroxyl radicals, thereby supporting the photodegradation of cationic IMI molecules.[60] Hence, higher pH levels than 10 did not favor the degradation process because alkaline media block the active sites of composites and preclude them from efficient degradation.

3.5.2. Effect of composite dose. The composite dosage has a significant influence on degradation; meanwhile, degradation depends upon the active sites present on the surface of the composite. The composite dosage effect was studied from 5 to 30 mg L^{-1} (Fig. 8C). The maximum degradation of IMI was obtained when a 5 mg L^{-1} dose of all composites was used. The degradation values at the optimum dose (5 mg L^{-1}) for PLN/CuO–NiO and PLN/Mn–Cu were 91% and 98%, respectively.[61] As the dosage amount was augmented from the optimum value, a decline in degradation efficiency of the nanoparticles occurred, owing to the agglomeration of composite particles, which covered the available active moieties, and reduced light penetration.[62] Additionally, at higher doses, all the active moieties become saturated with the establishment of equilibrium, and at this point, pesticide molecules are released back into the solution from the composite surface, leading to a decline in removal efficiency.[63]

3.5.3. Effect of contact time. Contact time is a crucial parameter that affects the percentage degradation of IMI under optimal conditions, which were studied from 5 to 150 min, and the output is depicted in Fig. 8D. The photocatalytic process necessitates the presence of O_2, H_2O, and light irradiation on the prepared composite surface to form electron–hole pairs.[64] At the start of the reaction, these bind to the surface of the composite due to a greater amounts, and the rate of degradation was initially very fast, then gradually slowed down, and finally reached the equilibrium values, indicating the saturation point. Experimental studies showed that the optimum time was 120 min for PLN/Mn–Cu and 60 min for PLN/CuO–NiO, having degradation capacities of 91% and 98%, respectively. As the reaction proceeds after the optimum time, all the available active sites become saturated, resulting in the unavailability of active sites; the already occupied binding sites repel the incoming pesticide molecules, and the rate of degradation becomes constant.[65]

3.5.4. Effect of imidacloprid concentration. The IMI concentration affects the degradation pathway due to the gradient factor and mass transfer. The effect of IMI concentration was assessed in the range of 2 to 12 mg L^{-1}, keeping other parameters constant (Fig. 8E). The sequestration efficiency increased as the initial concentration increased up to 6 mg L^{-1} *via* PLN/CuO–NiO, and after that, it decreased.[66] The optimum initial concentration point was 2 mg L^{-1} *via* PLN/Mn–Cu. It is due to the reason that at low initial pesticide concentration, the number of available active sites was high, and the removal capacity increased until the optimum point.[67] After that point, the diffusion of pesticide molecules to the composite surface becomes less efficient, resulting in a reduction in the generation of reactive species necessary for degradation, such as hydroxyl radicals, thereby reducing their availability for further degradation at higher concentrations. The IMI sequestration efficiency was recorded to be 84% and 87% using the given PBNCs, respectively.

3.6 Effect of oxidant dose

Hydrogen peroxide is an effective oxidant, and its combination with ultraviolet light or composites for the remediation of wastewater, has been demonstrated to be an innovative technology. The photocatalytic removal of IMI was studied in the absence and presence of H_2O_2 (at various concentrations), and the responses are shown in Fig. 9A.[68] A blank experiment was performed in the absence of H_2O_2 to analyze the degradation efficiency of IMI by PLN/Mn–Cu and PLN/CuO–NiO, which were found to be 59% and 54%, respectively. The role of H_2O_2 is to act as an electron acceptor and therefore has the capability to endorse charge separation and also yield OH^- through eqn (7):[69]

$$H_2O_2 + e^- \rightarrow OH^\bullet + OH^\bullet \qquad (7)$$

To elucidate the effect of the oxidant, the concentration of H_2O_2 was varied over a range of 5–20 mM. It has been observed that a significant improvement in the removal of IMI was demonstrated up to the optimum amount of 10 mM. At lower oxidant concentrations, the limited availability of scavengers (hydroxyl radicals and holes) allows recombination of photogenerated electrons and holes, thereby reducing the efficiency of pesticide degradation.[70] After the optimal concentration, there is a decline in the process. It is because at a higher amount of

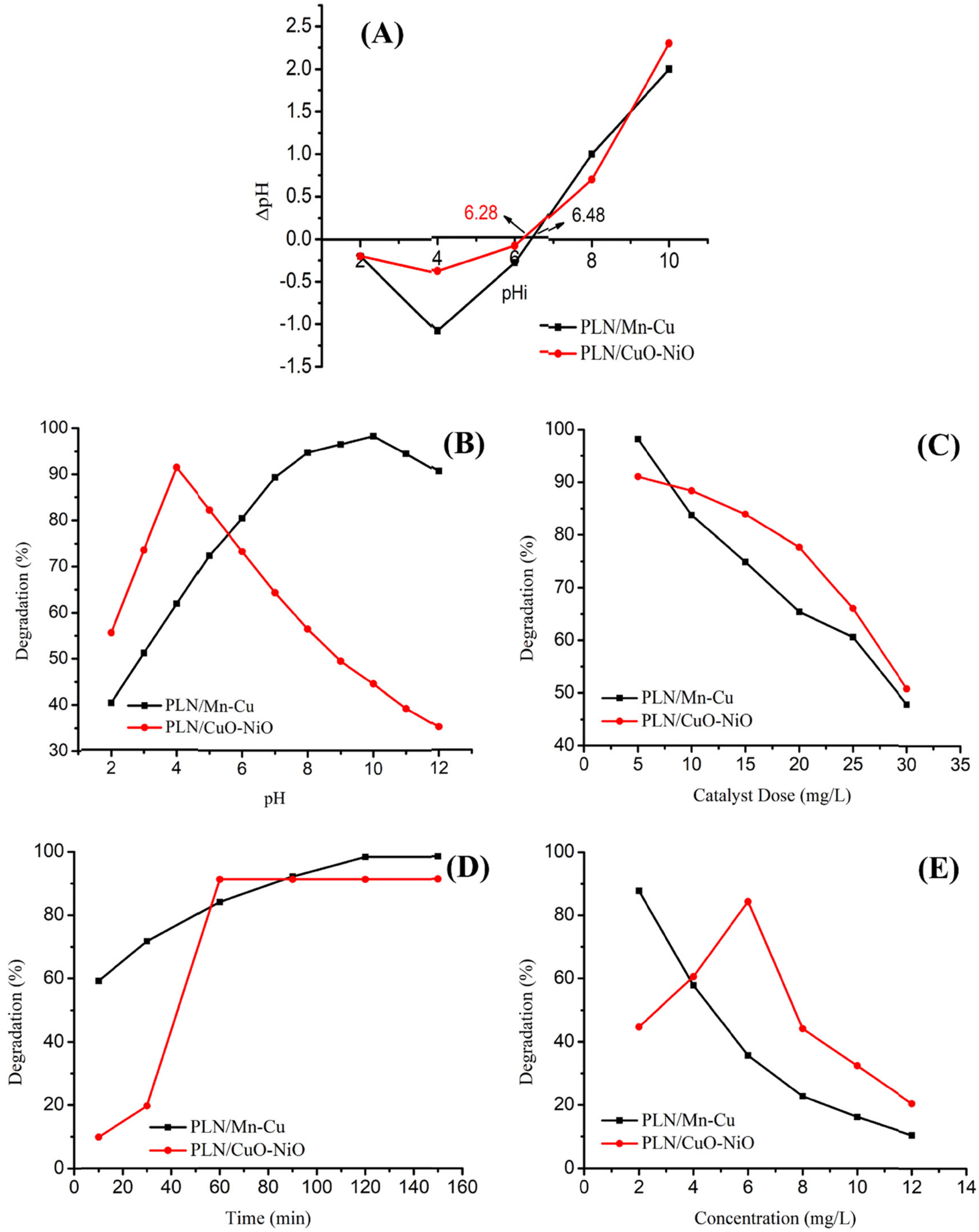

Fig. 8 (A) pHPZC measurement, (B) effect of pH, (C) effect of catalyst dose, (D) effect of irradiation time, and (E) effect of pesticide concentration on IMI photodegradation rate using PLN/Mn–Cu and PLN/CuO–NiO.

oxidant, the hydroxyl radical formed is converted into hydroperoxyl radicals, which decreases the penetration of UV light on the surface of the catalyst and reduces the rate of removal.[71] The production of hydroperoxyl radicals occurs as presented in eqn (8)–(11) and Fig. 10.

$$OH^{\bullet} + OH^{\bullet} \rightarrow H_2O_2 \quad (8)$$

$$H_2O_2 + OH^{\bullet} \rightarrow OH_2^{\bullet} + H_2O \quad (9)$$

$$OH_2^{\bullet} + OH_2^{\bullet} \rightarrow H_2O_2 + O_2 \quad (10)$$

$$OH^{\bullet} + O_2 \rightarrow OH_2^{\bullet} + O^{\bullet} \quad (11)$$

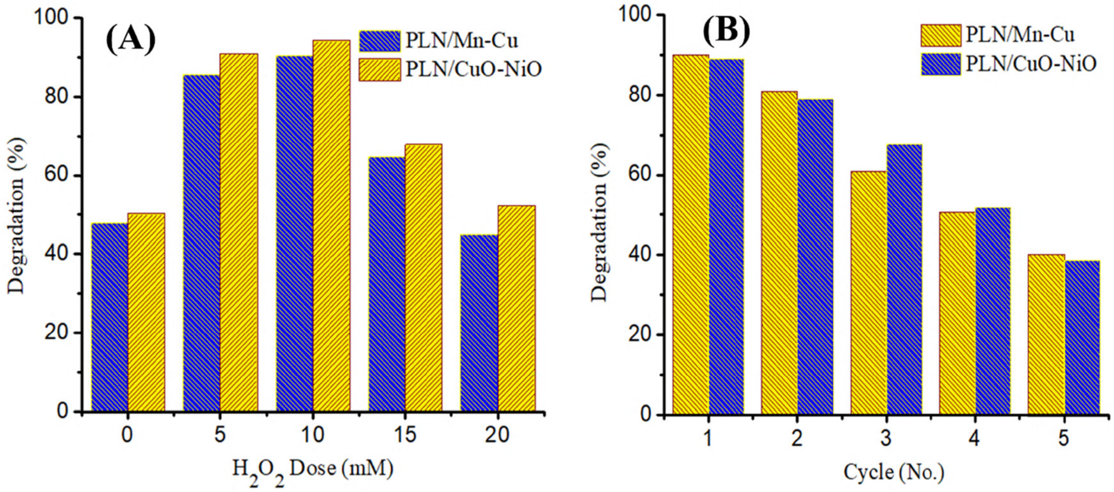

Fig. 9 (A) Effect of dosage on IMI removal using synthesized nanocomposites and (B) catalyst reusability and stability in five successive cycles for the photodegradation of IMI.

3.7. Reusability of catalyst

The reusability and stability of the PBNCs are economically important in removing pesticide pollutants from aqueous solutions by applying the optimal experimental conditions. The prepared catalysts were isolated from the solution after the first test, then thoroughly washed with distilled water and allowed to dry. The catalyst stability was evaluated in five cycles with an IMI concentration of 10 mg L^{-1} (Fig. 9B). After five cycles, the removal efficiency of IMI decreased from 98% and 91% to 38% and 35% *via* PLN/Mn–Cu and PLN/CuO–NiO, respectively.[72] This decrease in the catalytic activity of photocatalysts could be attributed to the following reasons: (1) material loss occurring in water in the recovery step after every cycle, which leads to a decrease in degradation performance;[73] (2) aggregation of nanoparticles causes a reduction in binding sites and effective surface area necessary for pesticide molecules to attach;[74] (3) obstruction of pores of active sites due to the development of intermediate molecules on the catalyst surface gradually decreases the removal efficacy.

3.8. Photocatalytic degradation mechanism

The charge transfer mechanism in the prepared nanocomposites under sunlight irradiation is shown in Fig. 10. When PLN/CuO–NiO and PLN/Mn–Cu nanocomposites are exposed to visible light, they absorb photons, which excite electrons to move from the valence band (VB) to the conduction band (CB), leaving holes in the VB. These composites are effective photocatalysts for visible light due to their small band gaps, specifically 2.13 eV and 2.15 eV, respectively. The CB potential for PLN/CuO–NiO is about −0.62 eV, and the VB is +1.51 eV compared to the NHE. Similarly, PLN/Mn–Cu has CB and VB values of −0.61 eV and +1.54 eV, respectively. The excited electrons (e^-) in CB break down surface adsorbed oxygen (O_2, $E^\circ = -0.33$ eV) to generate superoxide radicals ($O_2^{\bullet-}$). Subsequently, these radicals form hydrogen peroxide (H_2O_2) and then further hydroxyl radicals ($^\bullet$OH). At the same time, the holes (h^+) generated by light in the VB oxidize (oxidation potential greater than +1.23 eV) water (H_2O) or hydroxide ions (OH^-), producing further $^\bullet$OH radicals. These reactive oxygen species (ROS) are responsible for the degradation of imidacloprid.[75]

The nitrogen-rich imidacloprid molecule is oxidatively cleaved by $^\bullet$OH and $O_2^{\bullet-}$ attack, resulting in the formation of intermediate products like short-chain organic acids, urea-type fragments, and nitroso derivatives. These intermediates eventually mineralize into CO_2, H_2O, and nitrogen-containing species, such as NO_3^- and NH_4^+.[76] Additionally, the polyindole (PLN) coating increases the generation of reactive radicals and decreases electron–hole recombination by promoting improved charge separation and interfacial charge transfer. The existence of bimetallic CuO–NiO and Mn–Cu heterojunctions further supports efficient charge migration pathways. This may occur through either a Z-scheme mechanism, which separates electrons and holes while maintaining their potent redox ability, or a Type II heterojunction.[77] The charge carrier dynamics mechanism in PLN/composites during the photocatalytic degradation process is demonstrated by the reactions shown in eqn (12)–(18).

The pesticide solutions were examined under FTIR to track the metabolites and the success of the photodegradation process (Fig. 11).[78] The pristine IMI exhibited peaks at 3310 cm^{-1} due to the N–H stretching of the imidazolidine ring, which was masked by the O–H peak arising due to the presence of moisture. The peaks at 1529, 1415 and 1222 cm^{-1} correspond to the NO_2 stretching, C=C stretching and C=N stretching in the pyridine ring (Fig. 11a). The FTIR spectrum of aqueous solution of IMI showed a sharp peak at 3305 cm^{-1}, which is the characteristic peak of O–H stretching in water molecules (Fig. 11b). On complete degradation of the IMI molecules, most of the peaks disappeared, while some peaks at 3293 and 1637 cm^{-1} were observed for H–O–H stretching vibrations due to aqueous medium (Fig. 11c).[79] Based on the comparative data in Table 2, the present study demonstrates

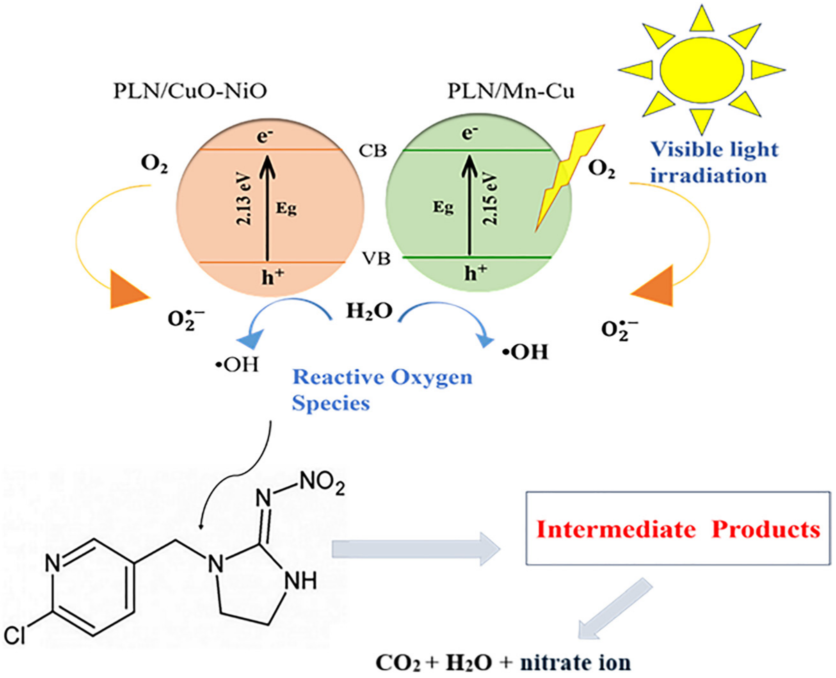

Fig. 10 Schematic of the photocatalytic degradation mechanism of imidacloprid.

several advantages over previously reported photocatalysts. While earlier systems such as PPY/CuO–NiO and Ni@$ZnO_{0.6}S_{0.4}$/SPID required longer irradiation times (180–300 min) to achieve moderate to high degradation efficiencies (83–90%), and ZnO/$CoFe_2O_4$ achieved rapid degradation (98% in 45 min) but at a higher catalyst dose, the PLN/Mn–Cu and PLN/CuO–NiO catalysts in this work achieved high degradation of imidacloprid (91–98%) under visible light with comparatively lower irradiation times (60–120 min). These results highlight the advantage of the present investigation in terms of efficient visible-light activity, shorter degradation times, and high pollutant removal rates, establishing the proposed PLN-based composites as highly effective and sustainable photocatalysts compared to previously reported systems.

$$\text{PLN/composites} + h\nu \rightarrow e^- + h^+ \tag{12}$$

$$h^+ + H_2O \rightarrow HO^\bullet + H^+ \tag{13}$$

$$h^+ + HO^- \rightarrow HO^\bullet \tag{14}$$

$$e^- + O_2 \rightarrow O_2^{\bullet -} \tag{15}$$

$$O_2^{\bullet -} + e^- + 2H^+ \rightarrow H_2O_2 \tag{16}$$

$$H_2O_2 \rightarrow 2HO^\bullet \tag{17}$$

$$h^+ + HO^\bullet + O_2^{\bullet -} + \text{IMI} \rightarrow CO_2 + H_2O + NO_3^- + NH_4^+ + Cl^- \tag{18}$$

3.9. Kinetic analyses

The algorithm designed for pseudo first (PFO), pseudo second order (PSO) and Behnajady–Modirshala–Ghanbery (BMG) kinetic models was employed on IMI sequestration data to determine the coefficient of determination (R^2) and their corresponding kinetic variable values (Fig. 12).[84] The order of reaction was estimated *via* the degree of fit, which was evaluated by the value of R^2, where a value close to 1 indicates complete alignment between the experimental data and the data obtained from kinetic models.[85] Through optimization of kinetic models, the rate constant of the reaction was determined *via* a linear regression equation. Commonly, the removal of organic pollutants from wastewater through advanced oxidation processes (AOPs) can be described by eqn (19).

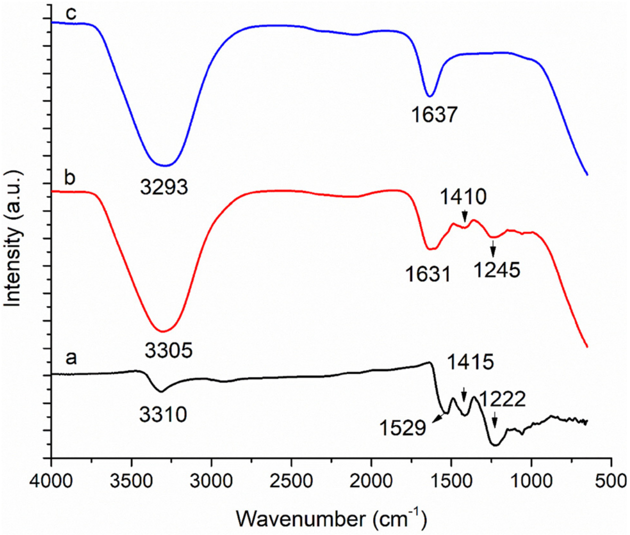

Fig. 11 FTIR spectra of (a) pristine IMI, (b) aqueous solution of IMI and (c) aqueous solution of IMI after degradation.

$$-\frac{dC}{dt} = k_1 C^n \tag{19}$$

Table 2 Comparison of the photocatalytic activities of PLN/Mn–Cu and PLN/CuO–NiO with those of other reported photocatalysts

Photocatalyst	Pollutant	Catalyst dose (g L^{-1})	Light source	Time (min)	Degradation (%)	Ref.
PPY/CuO–NiO	Alizarin red	0.1	Uv	300	86	24
PPY/CuO–ZnO	Metanil yellow	0.1	Vis	180	90	80
Gr-PLN	2,4-D	0.015	Uv	120	99	30
Ni@$ZnO_{0.6}S_{0.4}$/SPID	Bisphenol A	1	Vis	180	83	81
Mn–Cu_2O	Amoxicillin	1	Vis	180	92	82
ZnO/$CoFe_2O_4$	Imidacloprid	0.05	Vis	45	98	83
PLN/Mn–Cu	Imidacloprid		Vis	120	98	This work
PLN/CuO–NiO	Imidacloprid		Vis	60	91	This work

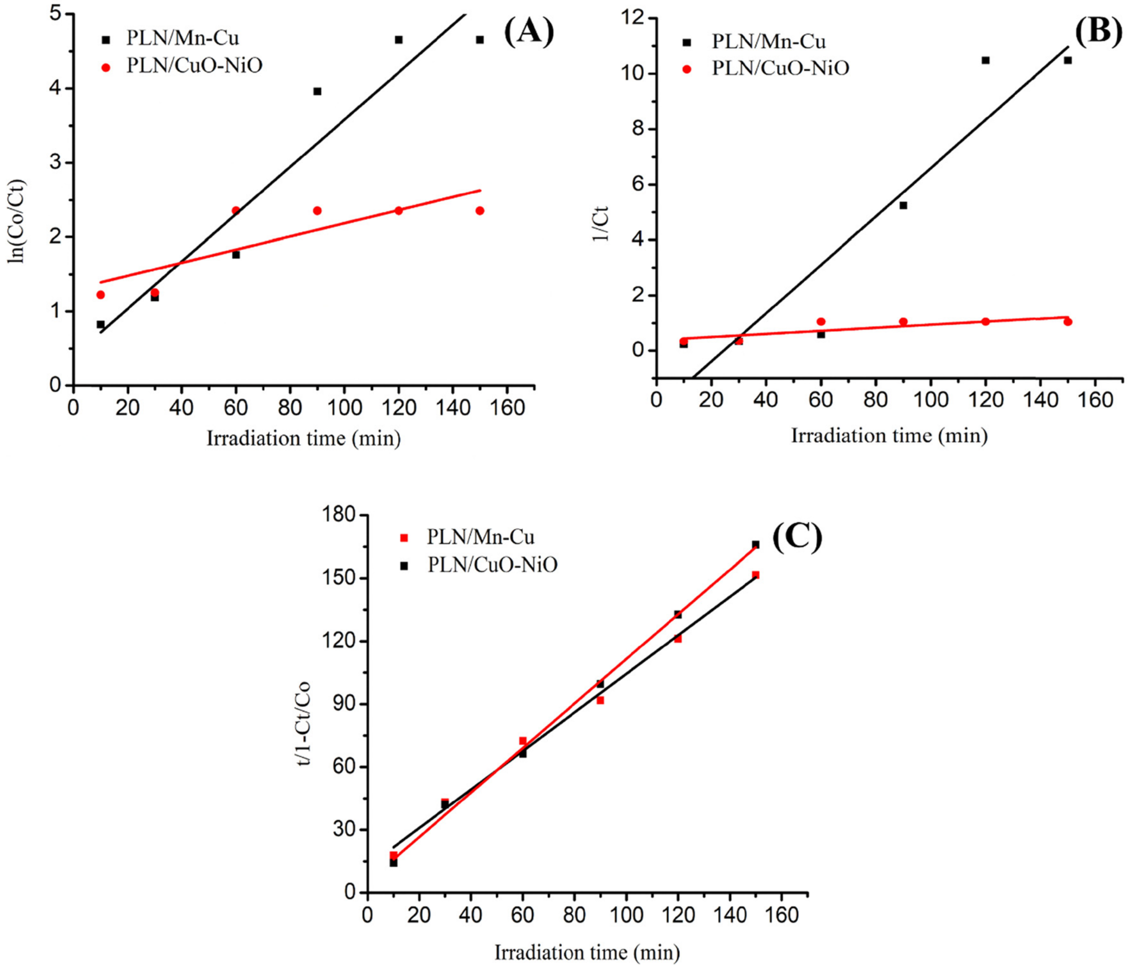

Fig. 12 Kinetic study: (A) pseudo first order, (B) pseudo second order and (C) BMG kinetic modelling of the photodegradation of IMI using PLN/Mn–Cu and PLN/CuO–NiO.

Here, C denotes pollutant concentration, k_1 = rate constant, t = time, and n = order of reaction and its value is 1 for a first-order reaction.[86] After integration, eqn (19) becomes eqn (20).

$$C_t = C_0 e^{-kt} \tag{20}$$

Taking natural logs on both sides:

$$\ln[C_t] = \ln[C_0] - k_1 t \tag{21}$$

Eqn (21) can be written as,

$$\ln\left(\frac{C_0}{C_t}\right) = k_1 t \tag{22}$$

This is the linear equation representing the PFO model. Here, C_0 and C_t denote IMI concentration at time t = 0 and concentration at t = t, respectively; k_1 is the rate constant and t is the reaction time. The plot of $\ln\left(\frac{C_0}{C_t}\right)$ *vs.* time gives the value of

Table 3 Kinetics variables for the removal of IMI using the synthesized composites

Kinetic parameters	PLN/Mn–Cu	PLN/CuO–NiO
Pseudo-first order		
k_1 (min^{-1})	0.032	0.001
R^2	0.919	0.675
Pseudo-second order		
k_2 (min^{-1})	0.087	0.006
R^2	0.889	0.674
BMG kinetic model		
m (min)	12.528	5.326
b	0.919	1.062
R^2	0.995	0.998

slope equal to the PFO rate constant (k_1). The R^2 values obtained after applying the PFO kinetic model were 0.919 and 0.675 for PLN/Mn–Cu and PLN/CuO–NiO, respectively, showing that the PFO kinetic model did not fit to the experimental data.[87] For second-order reactions, the value of n is 2.

$$-\frac{dC}{dt} = k_2C^2 \tag{23}$$

Hence, after integration and rearranging eqn (23) becomes eqn (24).

$$\frac{1}{C_t} = \frac{1}{C_0} + k_2t. \tag{24}$$

The plot between time and $1/C_t$ shows (Fig. 12) that the R^2 values of the PSO kinetic model were 0.889 and 0.674 for PLN/Mn–Cu and PLN/CuO–NiO, respectively. These values showed that the model was not suitable to describe the removal of pesticides.[88]

The kinetics of IMI pesticide can also be studied using the BMG model as defined in eqn (25).

$$\frac{t}{1-\frac{C_0}{C_t}} = m + bt \tag{25}$$

The plot of factor $t/1 - C_t/C_0$ *versus* time shows a straight line having an intercept value of m and a slope gives the value b. The kinetic data obtained from the BMG model indicated that R^2 values were 0.915 and 0.998 for PLN/Mn–Cu and PLN/CuO–NiO, respectively (Fig. 12). Hence, the BMG kinetic model shows high compatibility with the experimental data compared with other kinetic models in describing the removal of the IMI pesticide and is the best-fitting model.[89] The rate constants and R^2 values for IMI degradation *via* the photocatalytic process under optimized conditions are reported in Table 3.

4. Conclusion

In this study, for the first time, PLN/Mn–Cu and PLN/CuO–NiO, bimetallic nanocomposites of transition metals with embedded polyindole, were successfully synthesized *via* precipitation, hydrothermal and in situ-polymerization strategies and utilized for the removal of IMI from polluted water. The successful loading of PLN into these BNCs and efficient photoremoval of IMI into harmless substances was depicted by FTIR. The UV-visible study showed the reduction in the band gap of the prepared composite from 2.38 to 2.13 eV on the deposition of polymer. SEM indicated the morphology and average particle size of 118 and 75 nm, respectively. XRD analysis measured the crystal structure and average crystal size as 79 and 54 nm, respectively. Effect of numerous procedure parameters was premeditated, and the optimized circumstances were pH 4, composite dose 0.05 g, pesticide concentration 6 mg, H_2O_2 dose 10 mM and contact time 60 min for PLN/CuO–NiO. Similarly, the optimized conditions for PLN/Mn–Cu were pH 10, composite dose of 0.05 g, IMI concentration of 2 mg, H_2O_2 dose of 10 mM, and illumination time of 120 min, and the degradation efficiencies were found to be 91% and 98% for the PLN/Mn–Cu and PLN/CuO–NiO composites, respectively. A kinetic study demonstrated that the removal of IMI followed the BMG model using composites. The composite of CuO–NiO and Mn–Cu with PLN was efficient and could be used for the catalytic removal of the neonicotinoid insecticide IMI from polluted water and is also suitable for potential application in the remediation of other insecticides from effluents.

Conflicts of interest

The authors declare that they have no known competing financial interests or personal relationships that could have appeared to influence the work reported in this paper.

Data availability

The data used to support the findings of this study are available from the corresponding author upon request.

Acknowledgements

The authors express their gratitude to Princess Nourah bint Abdulrahman University Researchers Supporting Project number (PNURSP2025R11), Princess Nourah bint Abdulrahman University, Riyadh, Saudi Arabia.

References

1 H. Sukmana, N. Bellahsen, F. Pantoja and C. Hodur, *Prog. Agric. Eng. Sci.*, 2021, **17**, 49–68.
2 R. Akbar, H. N. Bhatti, M. Zahid and M. Y. Naz, *Environ. Sci. Pollut. Res.*, 2025, 1–25.
3 M. Lebiocka, A. Montusiewicz, M. Pawłowska, J. Ozonek, E. Szkutnik and M. Rosłan, *Arch. Environ. Prot.*, 2008, **34**, 63–70.
4 M. A. Hassaan and A. El Nemr, *Egypt. J. Aquat. Res.*, 2020, **46**, 207–220.
5 P. Rezende-Teixeira, R. G. Dusi, P. C. Jimenez, L. S. Espindola and L. V. Costa-Lotufo, *Environ. Pollut.*, 2022, **300**, 118983.
6 A. Intisar, A. Ramzan, T. Sawaira, A. T. Kareem, N. Hussain, M. I. Din, M. Bilal and H. M. N. Iqbal, *Chemosphere*, 2022, **293**, 133538.

7 M. P. Saini, *J. Healthcare Life-Sci. Res.*, 2023, **2**, 91–105.

8 L. Zuščíková, D. Bažány, H. Greifová, N. Knížatová, A. Kováčik, N. Lukáč and T. Jambor, *Toxics*, 2023, **11**, 598.

9 R. Guo, H. Zhang, C. Guo, N. Lv, B. Xi and J. Xu, *Chin. Chem. Lett.*, 2024, **35**, 109413.

10 M. Salemi and R. Brahimi, *Protective role of melissaspextract on neurological impacts of imidiacloprid in wistar rats*, Master's thesis, Universite laarbi tebessi tebessa, 2020.

11 Q. Kan, K. Lu, S. Dong, D. Shen, Q. Huang, Y. Tong, W. Wu, S. Gao and L. Mao, *Environ. Pollut.*, 2020, **267**, 115438.

12 H. Adabavazeh, A. Saljooqi, T. Shamspur and A. Mostafavi, *Polyhedron*, 2021, **198**, 115058.

13 M. Zangiabadi, A. Saljooqi, T. Shamspur and A. Mostafavi, *Ceram. Int.*, 2020, **46**, 6124–6128.

14 Q. Duan, S. Jiang, F. Chen, Z. Li, L. Ma, Y. Song, X. Yu, Y. Chen, H. Liu and L. Yu, *Ind. Crops Prod.*, 2023, **192**, 116075.

15 W. Kang, S. Chen, H. Yu, T. Xu, S. Wu, X. Wang, N. Lu, X. Quan and H. Liang, *J. Hazard. Mater.*, 2021, **405**, 124277.

16 A. Noor, S. R. M. Kutty, M. H. Isa, I. H. Farooqi, A. C. Affam, A. H. Birniwa and A. H. Jagaba, *The treatment of pharmaceutical wastewater*, Elsevier, 2023, pp. 217–245.

17 N. Arora, A. Kumar and S. K. Singal, *Measurement*, 2022, **190**, 110700.

18 K. Harby, M. Emad, M. Benghanem, T. Z. Abolibda, K. Almohammadi, A. Aljabri, A. Alsaiari and M. Elgendi, *Desalination*, 2024, 117600.

19 O. Scialdone, F. Proietto and A. Galia, *Curr. Opin. Electrochem.*, 2021, **27**, 100682.

20 D. R. Lobato-Peralta, E. Duque-Brito, A. Ayala-Cortés, D. M. Arias, A. Longoria, A. K. Cuentas-Gallegos, P. J. Sebastian and P. U. Okoye, *J. Environ. Chem. Eng.*, 2021, **9**, 105626.

21 V. R. Moreira, R. N. Guimarães, P. B. Moser, L. V. S. Santos, E. C. de Paula, Y. A. R. Lebron, A. F. R. Silva, G. S. Casella and M. C. S. Amaral, *J. Water Process Eng.*, 2023, **51**, 103450.

22 A. Bibi, S. Bibi, M. Abu-Dieyeh and M. A. Al-Ghouti, *J. Cleaner Prod.*, 2023, 137810.

23 J. Weng, J. Chen, Y. Xu, X. Hu, C. Guo, Y. Yang, J. Sun, L. Fu, Q. Wang and J. Wei, *J. Colloid Interface Sci.*, 2023, **652**, 1367–1380.

24 R. Biju, J. R. Vanaja Raghavan, R. Ravikumar and C. R. Indulal, *Plant Nano Biol.*, 2022, **2**, 100016.

25 M. Kumar, S. K. Samal and T. Maharana, *Polym. Technol. Mater.*, 2024, 1–20.

26 N. Chen, J. He, H. Xuan, J. Jin, K. Yu, M. Shi and C. Yan, *Composites, Part B*, 2024, **270**, 111145.

27 M. Atif Qaiyum, R. Kumari, J. Mohanta, P. P. Samal, S. Dutta, B. Dey and S. Dey, *J. Cluster Sci.*, 2023, **34**, 963–975.

28 C. Xie, L. Li, X. Zhai and W. Chu, *RSC Adv.*, 2023, **13**, 11069–11080.

29 L. Shao, P. Feng, Q. Liu, Y. Zhang, Z. Yu and S. Yan, *Constr. Build. Mater.*, 2024, **449**, 138294.

30 S. Ahmad, V. U. Siddiqui, A. Ansari, W. A. Siddiqi and M. K. Akram, *AIP Conference Proceedings*, AIP Publishing, 2020, vol. 2276.

31 J.-R. Li, W.-P. Zhang, C. Li and C. He, *J. Colloid Interface Sci.*, 2021, **591**, 396–408.

32 S. Anandhi, M. L. Edward and V. Jaisankar, *Mater. Today Proc.*, 2021, **40**, S93–S101.

33 A. Nigam, B. Singh, S. Saini, A. K. Rai and S. J. Pawar, *Inorg. Nano-Metal Chem.*, 2023, 1–11.

34 M. N. Tahir, K. S. Munawar, M. Feizi-Dehnayebi, M. Ashfaq and M. E. Muhammed, *J. Mol. Struct.*, 2024, **1297**, 136956.

35 S. J. Mohammed, K. M. Omer and F. E. Hawaiz, *RSC Adv.*, 2023, **13**, 14340–14349.

36 Q. Wei, G. Zhang and J. Xie, *Food Hydrocolloids*, 2024, **149**, 109599.

37 S. Taherkhani, F. Ghamari, J. Arjomandi, A. Nasri and H. Shi, *Fuel*, 2023, **353**, 129167.

38 H. Humayun, B. Begum, S. Bilal, A. ul H. A. Shah and P. Röse, *Nanomaterials*, 2023, **13**, 618.

39 E. Arulkumar, S. S. Shree and S. Thanikaikarasan, *Results Chem.*, 2023, **6**, 101087.

40 H. C. Sathisha, Anitha, G. Krishnamurthy, M. Pari, T. L. Soundarya and G. Nagaraju, *Chem. Data Collect.*, 2023, **48**, 101081.

41 G. Zhou, Y. Chen, G. Chen, H. Xu, W. Yin, B. Wang, X. Zhu, X. Ning, P. K. Chu and X. Wang, *Appl. Catal., B*, 2024, 124617.

42 N. O. Alafaleq, T. A. Zughaibi, N. R. Jabir, A. U. Khan, M. S. Khan and S. Tabrez, *Nanomaterials*, 2023, **13**, 1201.

43 Q. A. Alsulami and A. Rajeh, *Opt. Mater.*, 2022, **123**, 111820.

44 E. Arulkumar and S. Thanikaikarasan, *Optik*, 2024, **302**, 171685.

45 Z. Butt, M. Aamir, S. Aziz, J. Akhtar, A. Afaq, S. Naseer, Q. Wali, M. Nadeem and U. Jabeen, *Microsc. Res. Tech.*, 2023, **86**, 1132–1143.

46 Z. Nazeer, I. Bibi, F. Majid, S. Kamal, S. M. Ibrahim and M. Iqbal, *Opt. Mater.*, 2022, **125**, 112090.

47 M. Alzaid, A. M. Abu-Dief, N. M. A. Hadia, M. Ezzeldien and W. S. Mohamed, *Opt. Quantum Electron.*, 2024, **56**, 1–22.

48 Z. U. Rahman, U. Shah, A. Alam, Z. Shah, K. Shaheen, S. B. Khan and S. A. Khan, *Inorg. Chem. Commun.*, 2023, **148**, 110312.

49 F. Lopresti, F. C. Pavia, M. Ceraulo, E. Capuana, V. Brucato, G. Ghersi, L. Botta and V. La Carrubba, *J. Biomed. Mater. Res., Part A*, 2021, **109**, 2120–2136.

50 M. Ateia, G. Ersan, M. G. Alalm, D. C. Boffito and T. Karanfil, *Environ. Sci. Process. Impacts*, 2022, **24**, 172–195.

51 M. Iqbal, H. N. Bhatti, S. Noreen and S. Shukrullah, *Environ. Sci. Pollut. Res.*, 2024, 1–31.

52 H. R. Barai, N. S. Lopa, F. Ahmed, N. A. Khan, S. A. Ansari, S. W. Joo and M. M. Rahman, *ACS Omega*, 2020, **5**, 22356–22366.

53 H. Lv and H. Sun, *ACS Omega*, 2020, **5**, 11324–11332.

54 M. Bin Mobarak, M. S. Hossain, F. Chowdhury and S. Ahmed, *Arabian J. Chem.*, 2022, **15**, 104117.

55 S. Sajjad, A. Ikhlaq, F. Javed, S. W. Ahmad and F. Qi, *Water Sci. Technol.*, 2021, **83**, 727–738.

56 A. Kausar, S. Ijaz, M. Rafaqat, A. Dahshan, A. A. Latif, S. Bibi, N. S. Al-Kadhi, S. A. Alissa, A. Nazir and M. Iqbal, *J. Mol. Liq.*, 2023, **391**, 123347.

57 Y. Cheng, Z. Wang, J. Wang, L. Cao, Z. Chen, Y. Chen, Z. Liu, P. Xie and J. Ma, *J. Hazard. Mater.*, 2023, **441**, 129885.

58 D. Kathuria, M. Bhattu, A. Bankar and P. Puri, *Chemistry-Select*, 2023, **8**, e202302293.
59 A. Iqbal, A. ul Haq, L. Rios-Aspajo and A. Iturriaga-Chavez, *Glob. NEST J.*, 2023, **25**, 150–158.
60 K. Bano, S. Kaushal, B. Lal, S. K. Joshi, R. Kumar and P. P. Singh, *Environ. Nanotechnol., Monit. Manage.*, 2023, **20**, 100863.
61 M. Ta, T. Wang, J. Guo, Y. Wang, J. Zhang, C. Zhao, S. Liu, G. Liu and H. Yang, *Sep. Purif. Technol.*, 2023, **310**, 123067.
62 Y. Zou, Y. Hu, Z. Shen, L. Yao, D. Tang, S. Zhang, S. Wang, B. Hu, G. Zhao and X. Wang, *J. Environ. Sci.*, 2022, **115**, 190–214.
63 M. Ortiz-Martínez, B. Restori-Corona, L. Hernández-García and D. Alonso-Segura, *Macromol*, 2024, **4**, 785–804.
64 S. Porcu, F. Secci and P. C. Ricci, *Molecules*, 2022, **27**, 6828.
65 C. Yang, H.-R. Yang, S.-S. Li, Q.-D. An, S.-R. Zhai and Z.-Y. Xiao, *J. Colloid Interface Sci.*, 2022, **625**, 651–663.
66 A. Derbalah, M. Sunday, R. Chidya, W. Jadoon and H. Sakugawa, *J. Water Health*, 2019, **17**, 254–265.
67 Y. Yang, X. Ma, Z. Li, Y. Wang, C. Ju, L. Cao, Y. Zheng and Q. Zhang, *Chem. Eng. J.*, 2023, **465**, 142788.
68 R. Saleh, S. A. Hidayat, A. Taufik and S. Yin, *Arabian J. Chem.*, 2022, **15**, 103881.
69 S. Qu, H. Wu and Y. H. Ng, *Adv. Energy Mater.*, 2023, **13**, 2301047.
70 M. Althamthami, E. Guettaf Temam, H. Ben Temam, G. G. Hasan and N. Malfi, *Ceram. Int.*, 2022, **48**(21), 31570–31578.
71 M. N. Arifin, R. Jusoh, H. Abdullah, N. Ainirazali and H. D. Setiabudi, *Environ. Res.*, 2023, **229**, 115936.
72 F. Ma, Y. Wang, Z. Fu, Y. Tang, J. Dai, C. Li and W. Dong, *Constr. Build. Mater.*, 2022, **335**, 127494.
73 A. A. Fauzi, A. A. Jalil, N. S. Hassan, F. F. A. Aziz, M. S. Azami, T. A. T. Abdullah, M. F. A. Kamaroddin and H. D. Setiabudi, *Environ. Res.*, 2022, **211**, 113069.
74 H. Karimi-Maleh, M. Ghalkhani, Z. S. Dehkordi, J. Singh, Y. Wen, M. Baghayeri, J. Rouhi, L. Fu and S. Rajendran, *J. Ind. Eng. Chem.*, 2024, **129**, 105–123.
75 H. Shi, W. Wang, L. Mao, L. Zhang, L. Zhu, C. Wu and X. Liu, *J. Environ. Manage.*, 2025, **380**, 124929.
76 A. H. Zyoud, S. H. Zyoud and S. H. Zyoud, *Appl. Water Sci.*, 2025, **15**, 159.
77 W. Zhang, D. Liu, Z. Mu, X. Zhang, G. Dong, L. Bai, R. Guo, J. Li, M. Zhao and Z. Zhang, *J. Inorg. Organomet. Polym. Mater.*, 2023, **33**, 90–104.
78 S. G. Mohammad and A. A. El-Refaey, *J. Water Land Dev.*, 2023, 220–230.
79 A. Khan, Z. A. Raza, H. N. Bhatti and T. Sarwar, *Int. J. Biol. Macromol.*, 2024, **261**, 129881.
80 R. Biju, R. Ravikumar, C. Thomas and C. R. Indulal, *J. Nanopart. Res.*, 2022, **24**, 117.
81 A. D. Ali, S. H. Ammar and E. M. Khudhair, *Environ. Nanotechnol., Monit. Manage.*, 2020, **14**, 100359.
82 Y. T. Gaim, S. M. Yimanuh and Z. G. Kidanu, *J. Compos. Sci.*, 2022, **6**, 317.
83 M. Naghizadeh, M. A. Taher and A.-M. Tamaddon, *Heliyon*, 2019, **5**(11), e02870.
84 A. G. A. Reyad, G. I. K. Marei, M. A. Abbassy, E. I. Rabea and M. E. I. Badawy, *Int. J. Mod. Agric. Environ.*, 2023, **3**, 29–48.
85 R. Juturu, V. R. Murty and R. Selvaraj, *Chemosphere*, 2024, **349**, 140731.
86 M. Tang, J. Wan, Y. Wang, Z. Yan, Y. Ma, J. Sun and S. Ding, *Chem. Eng. J.*, 2022, **445**, 136755.
87 X. Ji, Y. Liu, Z. Gao, H. Lin, X. Xu, Y. Zhang, K. Zhu, Y. Zhang, H. Sun and J. Duan, *Sep. Purif. Technol.*, 2024, **330**, 125235.
88 J. Kumar, P. Kaur, D. Sud, A. Saini and P. Bansal, *Mater. Today Proc.*, 2023, **78**, 849–857.
89 P. Butcherine, B. P. Kelaher and K. Benkendorff, *Aquat. Toxicol.*, 2022, **242**, 106050.